Materials & Design 221 (2022) 110976

Contents lists available at ScienceDirect

Materials & Design

journal homepage: www.elsevier.com/locate/matdes

Excellent strength–ductility balance of Sc-Zr-modified Al–Mg alloy by tuning bimodal microstructure via hatch spacing in laser powder bed fusion

Yusufu Ekubaru [a,b], Ozkan Gokcekaya [a,b], Takuya Ishimoto [a,b,c], Kazuhisa Sato [d], Koki Manabe [a], Pan Wang [e], Takayoshi Nakano [a,b,*]

[a] Division of Materials and Manufacturing Science, Graduate School of Engineering, Osaka University, 2-1 Yamadaoka, Suita, Osaka 565-0871, Japan
[b] Anisotropic Design and Additive Manufacturing Research Center, Osaka University, 2-1, Yamadaoka, Suita, Osaka 565-0871, Japan
[c] Aluminium Research Center, University of Toyama, 3190, Gofuku, Toyama 930-8555, Japan
[d] Research Center for Ultra-High Voltage Electron Microscopy and Division of Materials and Manufacturing Science, Graduate School of Engineering, Osaka University, Ibaraki 567-0047, Japan
[e] Singapore Institute of Manufacturing Technology, A*STAR, 73 Nanyang Drive, 637662, Singapore

HIGHLIGHTS

- Microstructural control utilizing bimodal feature unique to LPBF-built Scalmalloy.
- Decreasing track-to-track interval increases the volume fraction of fine grains.
- The increased volume fraction of fine grains resulted in increased strength.
- The resulting product exhibited an excellent strength-ductility balance.

GRAPHICAL ABSTRACT

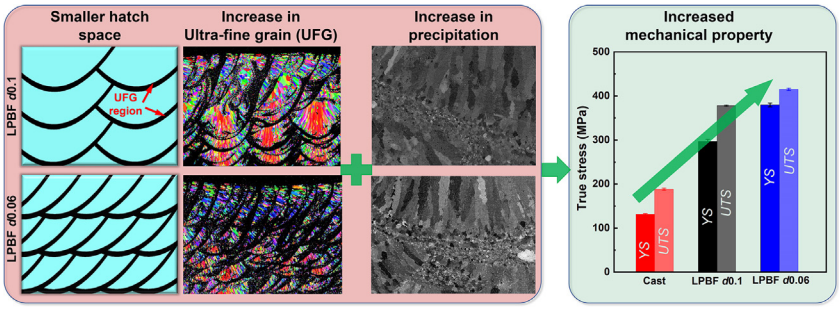

ARTICLE INFO

Article history:
Received 25 May 2022
Revised 6 July 2022
Accepted 20 July 2022
Available online 22 July 2022

Keywords:
Scalmalloy
Laser powder bed fusion
Ultrafine grain
Hatch spacing
Melt pool
Precipitation

ABSTRACT

The bimodal microstructure, which comprises ultrafine grains (UFGs) forming along the melt pool boundary and relatively coarse grains inside the melt pool, is a characteristic of the Sc-Zr-modified Al–Mg-based alloy (Scalmalloy) microstructure manufactured using laser powder bed fusion (LPBF). Focusing on this microstructural feature, we investigated the improvement in the mechanical properties of LPBF-fabricated Scalmalloy by tailoring the volume fraction of UFGs. Our approach was to decrease the laser hatch spacing (d) from 0.1 to 0.04 mm, while the volume fraction of UFGs increased from 34.6 ± 0.6 % (d = 0.1 mm) to 59.5 ± 0.5 % (d = 0.06 mm). The tensile yield stress increased from 296 ± 9 (d = 0.1 mm) to 380 ± 6 MPa (d = 0.06 mm), while maintaining a large elongation (14.8 % ± 1.2 %). The yield stress and elongation were superior to those of the cast counterparts by 2.9 and 4.0 times, respectively. In the sample with d = 0.04 mm, pores formed owing to excessive thermal energy input. Additionally, we investigated multiple strengthening mechanisms of the as-fabricated alloy. This is the first study to improve the mechanical properties of LPBF-fabricated Scalmalloy by optimizing the track-to-track interval and tuning the UFG fraction.

* Corresponding author.
E-mail address: nakano@mat.eng.osaka-u.ac.jp (T. Nakano).

https://doi.org/10.1016/j.matdes.2022.110976
0264-1275/

1. Introduction

There is large demand for high-performance, light-weight, strong metal products with high structural complexity, ductility, and short design and production periods in many industries, such as the space, aerospace, biomedical, and automotive industries. Because laser powder bed fusion (LPBF)–based additively manufactured products can satisfy these requirements, they have recently received considerable research interest [1–3]. Compared to conventional metal processing technologies, such as casting, joining, and injection molding, LPBF offers many unique advantages, such as a short time to market, design freedom, and high resolution and accuracy. These advantages facilitate the manufacturing of complex geometries while controlling the microstructure by adjusting the laser beam parameters, such as power (P), scanning speed (v), laser hatch spacing (d), powder layer thickness (h), and scan strategy [4]. The production quality depends on the heat transfer mechanism, temperature distribution, and melt pool formation in the powder bed, which are directly influenced by the laser beam parameters. Thus, finding an appropriate combination of the parameters required to obtain an optimized microstructure for LPBF is challenging. Specifically, numerous metallic alloys used today cannot be manufactured through LPBF because the melting and solidification dynamics of the fabrication process conducted at a rapid cooling rate ($\sim 10^6$ K/s) lead to the formation of undesirable microstructures, such as cracks and hot tears [5]. Currently, stainless steel [6–8], Ti-based alloys [9,10], Ni-based alloys [11,12], and Al-based alloys [13–15] are fabricated by LPBF. Al-based alloys include near-eutectic Si-containing alloys, such as AlSi12 [16] and AlSi10Mg [17], and Sc- and/or Zr-modified Al-Mg-based alloys (typically referred to as Scalmalloy) have been applied for the LPBF process [18,19]. The Sc addition in Al-alloy generates a nanoscale phase of Al_3Sc, which plays a significant role in grain refinement, raising the recrystallization temperature, increasing the temperature strength and corrosion resistance, and preventing embrittlement. These are intrinsic characteristics and advantages of Scalmalloy compared with other Al alloys [20].

Research on the LPBF of Scalmalloy has revealed that the microstructure of Scalmalloy has two distinct grain structure regimes, which are referred to as bimodal microstructures, namely, coarse grains (CGs) in hot melt pool areas with temperatures > 800 °C [19] and ultrafine grains (UFGs) along the melt pool boundaries (MPBs). The larger CGs are located in the hot melt pool areas and are oriented toward the melt pool center along the thermal gradient. The formation of UFG regions is primarily attributed to the remnants of the considerable Al_3(Sc, Zr) heterogeneous nucleation at the MPBs, whereas that of CG regions is attributed to the lack of Al_3(Sc, Zr) precipitation resulting from the high-temperature gradients toward the melt pool surface [19–21]. Additionally, research on the strengthening mechanisms of Al–Mg–Sc–Zr alloys revealed that the primary contributors to alloy strength are the formation of UFGs (grain boundary strengthening); solid solution strengthening and precipitate strengthening [22], while grain boundary strengthening also contributed. The previous strategy, which was combined with increasing remelting zone volume and decreasing thermal gradient, was used to increase the fraction of UFGs [20]. The formation of UFGs was due to the presence of large amounts of Al_3(Sc, Zr) particles in the remelting zone. Therefore, it was proposed that increasing the remelting zone volume by increasing the laser energy density can increase the UFG [20]. Furthermore, LPBF fabricates components using a high-energy laser to selectively melt fine metal powders layer by layer, and this causes the overlapping of the multi-track and multi-layer melt pools of the metal powders. Two types of MPBs are therefore formed in LPBF parts, layer–layer and track–track [23]. Accordingly, it is assumed that the volume fraction of UFGs and precipitation can be increased by increasing the volume fraction of MPBs. The increments of MPBs in the LPBF process can be realized using a small d because a small d increases the laser spot overlap and leads to the overlapping of the melt pool, increasing track–track MPBs. Further, it is known that Al_3(Sc, Zr) precipitates form during not only the LPBF-solidification process but also the aging treatment process [24,25]. A smaller d can also promote the aging process by increasing the heat from thermal cycling [26]. Therefore, it was assumed that a small d can activate multi-strengthening mechanisms, i.e., a smaller d can increase the volume fraction of UFGs by increasing track–track MPBs, which simultaneously improve precipitation strengthening by promoting the aging effect. However, a small d can impart high porosity and/or induce the evaporation of some of the elements because of the high temperature and instability of the melt pools caused by the high laser energy density (E) input [27]. To overcome these issues, in this study, the laser parameters were set to the reported optimal range of E = 77–238 J mm^{-3} [18,19]. The values of E outside this range might cause melt pool instability or significant evaporation issues. The laser power, scan speed, scan strategy, and baseplate temperature were studied as process parameters [20]. However, the effect of d on the bimodal grain structure has not been investigated, although a decrease in d promotes the formation of track-track MPB, thus increasing the possible formation of UFGs. To the best of our knowledge, this is the first study to adopt a small d as an effective parameter to promote UFG formation, given the nature of Scalmalloy.

This study aimed to extend our knowledge on the effect of hatch spacing (d) on the microstructure of LPBF-manufactured Scalmalloy, to enhance mechanical properties by promoting UFG and precipitate formation. The as-built Scalmalloy samples were characterized using porosity and microstructural analyses, hardness measurements, and tensile tests. Moreover, this study demonstrated that a smaller d can enhance the capacity of multiple strengthening mechanisms of Scalmalloy, illustrating the improvement in mechanical properties.

2. Experimental procedure

2.1. Scalmalloy fabrication

The Scalmalloy powders used in this study (under the name SCALMA40B5) were procured from Toyo Aluminium K. K. (Japan); their compositions and morphologies are summarized in Table 1 and shown in Fig. 1(a), respectively. For convenience, SCALMA40B5 is hereinafter referred to as Scalmalloy. The particle size distribution of Scalmalloy, shown in Fig. 1(b), was measured using a Mastersizer 3000E particle size analyzer (Malvern Panalytical, UK). The avalanche angle and surface fractal were analyzed using a Revolution powder analyzer (Mercury Scientific, USA) to assess the flowability and estimate the homogeneity of the powder bed.

An LPBF machine (EOS M290, Germany) with a 400 W Yb-fiber laser and a beam diameter of 100 μm was used to prepare the Scalmalloy samples. As shown in Fig. 1(c), the 5 mm × 5 mm × 15 mm samples, along the x-, y-, and z-axes, respectively, were fabricated on an Al baseplate using bidirectional laser scanning in the x-direction. In addition, 5 mm × 5 mm × 30 mm samples were fabricated for tensile testing. The parameter d was set successively to 0.1, 0.08, 0.06, and 0.04 mm, and the corresponding samples are hereinafter referred to as d0.1, d0.08, d0.06, and d0.04, respectively. The calculated volumetric energy densities ($E = P/(vdh)$) are listed in Table 2. The building stage was preheated to 35 °C, and the building chamber was filled with high-purity Ar gas to maintain an O_2 content below 100 ppm.

Table 1
Chemical composition (wt%) of Scalmalloy.

Powder	Al	Mg	Sc	Zr	Mn	Fe	Si	Ti
SCALMA40B5	Bal.	4.8	0.74	0.29	0.57	0.10	0.04	0.02

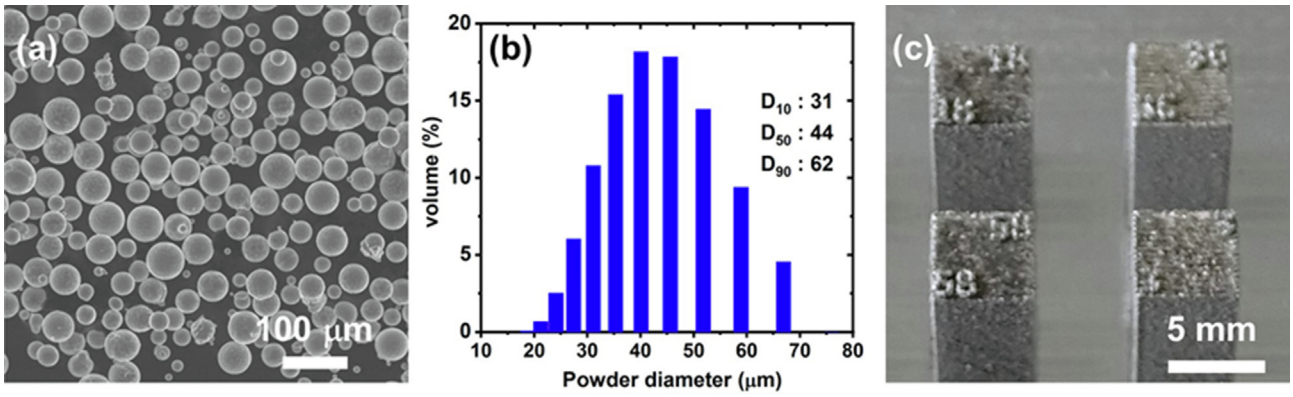

Fig. 1. (a) Morphology of the Scalmalloy powders used in LPBF, (b) powder size distribution, and (c) appearance of the LPBF-fabricated samples.

Table 2
Laser parameters, yield stress, UTS, elongation, and Vickers hardness of the samples.

d (mm)	*P* (W)	*v* (mm/s)	*E* (J/mm^3)	Yield stress (MPa)	UTS (MPa)	Elongation (%)	Hardness ($Hv_{0.1}$)
0.1	360	600	100	296 ± 9	378 ± 2	23.1 ± 2.5	105 ± 2
0.08	360	600	125	301 ± 4	357 ± 2	18.7 ± 2.1	113 ± 3
0.06	360	600	166	380 ± 6	415 ± 4	14.8 ± 1.2	132 ± 4
0.04	360	600	250	358 ± 5	388 ± 7	13.2 ± 1.9	118 ± 7
Casting [34]	–	–	–	131 ± 2	188 ± 2	3.7 ± 0.6	–

2.2. Microstructure characterization and mechanical properties

Samples were cut from the substrate using electrical discharge machining to investigate the microstructures and mechanical properties. The YZ, XZ, and XY cross sections were mechanically polished using emery paper up to 4000-grade and then chemically polished using colloidal silica to obtain mirror-polished sections for microstructural observation. Optical microscopy (BX60, Olympus, Japan) and field emission scanning electron microscopy (FE-SEM; JIB-4610F, JEOL, Japan) were used to examine the microstructures. Crystallographic texture analysis was conducted using electron backscattered diffraction (EBSD; NordlysMax^3, Oxford Instruments, UK) mounted on FE-SEM at an accelerating voltage of 20 kV and a step interval of 0.5 μm. The data obtained were analyzed using analysis software (Aztec HKL, Oxford Instruments, UK) to obtain inverse pole figure maps and corresponding pole figures. The average chemical composition was investigated via energy-dispersive X-ray spectroscopy (EDS; Aztec 3.1, Oxford Instruments, UK) mounted on FE-SEM.

The chemical composition of nanoprecipitation in Scalmalloy was characterized using scanning transmission electron microscopy (STEM; JEM-ARM200F, JEOL, Japan) operating at 200 kV combined with EDS (JED-2300, JEOL, Japan). For STEM imaging, the beam convergence was set to a semi-angle of 23 mrad, and high-angle annular dark-field (HAADF) images were acquired with detector semi-angles in the range of 68–170 mrad.

Vickers hardness was measured using a Vickers hardness tester (HMV-G31-FA, Shimadzsu, Japan) with a 100 g load for 15 s. The test was conducted seven times for the YZ plane of each sample, and the results were averaged. Tensile specimens with a gauge of 5 mm length, 1.1 mm width, and 0.7 mm thickness were prepared. The tensile test (AGX-50kNV, Shimadzu, Japan) was conducted in vacuum at room temperature at an initial strain rate of 1.67×10^{-4} s^{-1}, where the loading axis was parallel to the build direction (BD). The test was conducted three times for each hatch spacing, *d*, and the results were averaged.

2.3. Analysis of the volume fraction of UFGs and precipitates

The volume fractions of the UFGs and precipitates were calculated based on the EBSD band contrast and SEM backscattered electron (BSE) images using the Mathematica image processing program developed by the authors.

2.4. Statistical analyses

The significance of *d*-dependent changes was tested using one-way analysis of variance (ANOVA). Post hoc Tukey's honest significant difference or Games–Howell comparisons were conducted according to the test for homoscedasticity. Statistical significance was set at $P < 0.05$. SPSS version 25.0 J (SPSS Japan Inc., Tokyo, Japan) for Microsoft Windows was used to perform the statistical analyses.

3. Results

The Scalmalloy powders were spherical in shape with fewer satellite, as shown in Fig. 1(a). The volume-weighted percentiles of the Scalmalloy powder were D_{10} = 31, D_{50} = 44, and D_{90} = 62 μm. The avalanche angle and surface fractal of the Scalmalloy powder were 40.4° and 1.94°, respectively, indicating a

good flowability [28]. A powder with adequate flowability is expected to have a low avalanche angle and a surface fractal close to one [29].

Fig. 2 shows the optical microstructures of the LPBF-fabricated samples. The microstructures of the samples, except for sample *d*0.04, were dense with no visible cracks, and they achieved a sufficient industrial density of > 99.5 % [5,46]. However, noticeable spherical pores were present in sample *d*0.04, which significantly reduced the density (99.20 ± 0.23 %) ($P < 0.05$ by Tukey's test).

The bimodal grain microstructures of Scalmalloy consisting of UFG and CG regions can be explained by the schematic of the melt pool, shown in Fig. 3; clearly, the surrounding thick bands correspond to the MPBs comprising the UFGs due to Al_3(Sc, Zr) precipitation. The two thick black curves at the bottom and top of the melt pool, which were generated from layer-by-layer overlapping, are called layer–layer MPBs. Moreover, the two thick gray bands at the two sides of the melt pool, which were generated from track-by-track overlapping, are referred to as track–track MPBs, which further promote UFG formation [23]. The elongated CGs nucleated from the layer–layer MPBs, while the UFGs on the MPBs nucleated from Al_3(Sc, Zr) precipitation. We propose that the decrease in *d* is an effective approach to promote track–track MPB formation and increase the UFG ratio.

EBSD analysis was conducted on the YZ plane of the final scanning layers to observe the variation in the MPBs with decreasing *d*. This allowed the observation of the uppermost part of the melt pools without the influence of the next scan layer. Fig. 4(a)–4(d) schematically illustrate MPBs with UFGs shown as black lines; clearly, the volume fraction of UFGs increases with decreasing *d*. Fig. 4(a')–4(d') show the band contrast images indicating the characteristic bimodal microstructure comprising darker and lighter regions. The darker regions at the MPBs correspond to UFGs with a size of < 2 μm, and the lighter regions in the melt pools correspond to CGs with a size of > 2 μm [19]. These experimental results demonstrate that the strategy of increasing the number of UFGs using a small *d* is effective. The inverse pole figure maps in Fig. 4 (a″)–4(d″) show that the CGs oriented in the BD (Z-direction) decreased with decreasing *d*.

Fig. 5 shows the EBSD inverse pole figure maps, pole figures, volume fractions of UFGs and the schematics of the melt pool shapes projected on the YZ, XZ, and XY planes. Fig. 5(a)–5(d) show the crystallographic orientation maps projected along the BD (z-direction) and recorded in the YZ plane, which is perpendicular to the scan direction. The CGs grew along the thermal gradient direction toward the top center of the melt pool. The growth direction of the CGs corresponded to the {1 0 0} crystallographic direction, which is an easy growth direction for the FCC crystal structure [4]. However, these CGs could not continuously grow to the subsequent layer because of the formation of UFGs at the MPBs. The UFGs were randomly oriented and primarily formed as a result of Al_3(Sc, Zr) precipitation. The volume fraction of UFGs increased from sample *d*0.1 to sample *d*0.06; however, it decreased slightly for sample *d*0.04. Consequently, the maximum volume fraction of the UFGs (approximately 60 %) was detected for sample *d*0.06 (Supporting Fig. S1). The pole figure of the samples showed that a weak (1 0 0) fiber texture appeared in sample *d*0.1; however, the intensity of the texture decreased with decreasing *d* owing to the increase in the UFG ratio, as indicated in Fig. 5. Fig. 5(a')–5(d') and Fig. 5(a″)–5(d″) show the crystallographic orientation maps projected along the BD and recorded in the XZ and XY planes, respectively. The distribution of UFGs corresponds to the melt pool shape. The grain size was calculated from the EBSD band contrast images in Fig. 5. The UFG sizes were 1.48 ± 0.16, 1.26 ± 0.18, 1.05 ± 0.14, and 1.08 ± 0.17 μm for samples *d*0.1, *d*0.08, *d*0.06, and *d*0.04, respectively. Note that the volume fraction of UFGs increased from 34.6 ± 0.6 % (*d* = 0.1) to 59.5 ± 0.5 % (*d* = 0.06) ($P < 0.05$ by Games-Howell test) without grain growth along with the decrease in *d* from 0.1 to 0.06 mm.

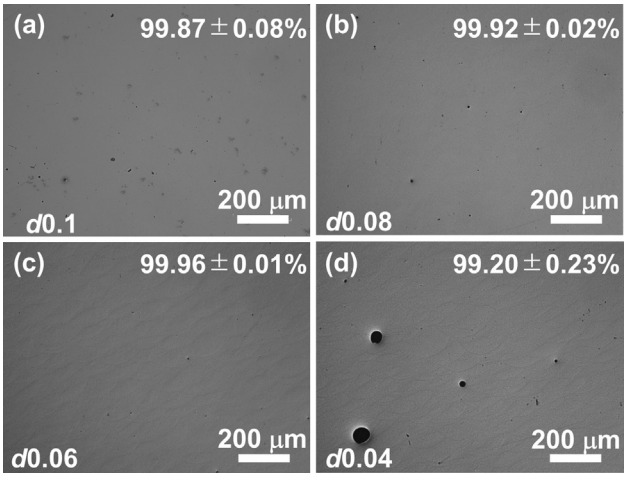

Fig. 2. Optical microscopy images and the corresponding optical density.

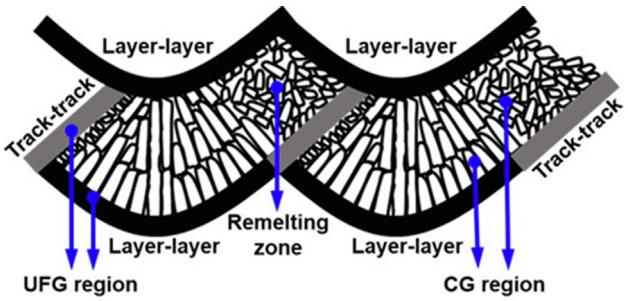

Fig. 3. Schematic of the cross section of Scalmalloy grain formation in the melt pool during the LPBF process.

X-ray diffraction (XRD) analysis was conducted on the polished XY cross section of the samples to confirm the existence of second phases. The cross-sectional XRD patterns of the LPBF-fabricated Scalmalloy together with the reference peak position of pure Al (JCPDS Card No. 01-073-2661) are shown in Fig. 6(a). The enlarged figure of the peaks at $2\theta = 38.3°$ and 44.6° shows that each peak is divided into two peaks, namely, the main Al peak and a smaller peak corresponding to Al_3(Sc, Zr) [25]. Furthermore, the relative intensities of the (1 1 1) and (2 0 0) peaks were similar, although (1 1 1) is the highest-intensity peak, suggesting that the (1 0 0) tended to orient in the BD (z-direction), which is consistent with the EBSD results. Interestingly, a slight peak shift to a lower diffraction angle occurred for samples *d*0.08 and *d*0.06, whereas the diffraction angle recovered to the standard value for *d*0.04. This could be attributed to the differences in the residual stress of the samples [25]. Furthermore, it has been reported that higher *E* values cause an increase in residual stress [9,30]. Although the peak shifts of samples *d*0.08 and *d*0.06 corresponded to an increase in laser *E*, sample *d*0.04 exhibited recovery from residual stress due to the aging effect of the small *d*.

Fig. 6(b), which shows a high-resolution TEM image at a zone axis of $[11\,\bar{2}]_{FCC}$, confirms the existence of the $L1_2$ phase. Fig. 6(c) shows the fast Fourier transform pattern obtained from the $L1_2$ region. A cube-on-cube relationship exists between the fcc Al matrix and $L1_2$ Al_3(Sc, Zr) precipitates. To clarify the distribution of the precipitates, the SEM-BSE images were examined for all as-built samples.

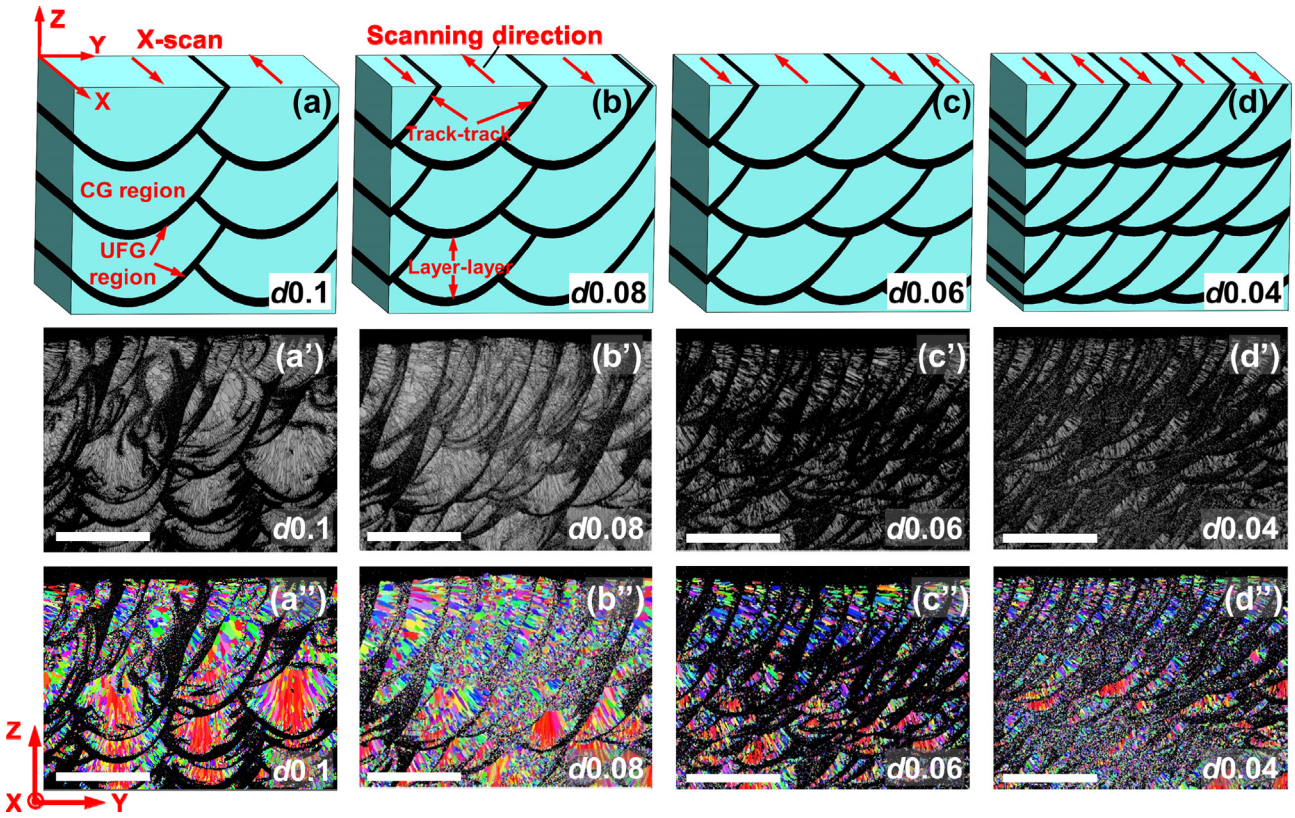

Fig. 4. (a)–(d): Three-dimensional schematics of MPBs and the resultant UFG configuration; (a')–(d'): EBSD band contrast images and (a")–(d") inverse pole figure maps obtained from the topmost part of the samples. All micrographs were acquired in the YZ plane. Scale bars: 200 μm.

The BSE images of the YZ plane of the as-built Scalmalloy samples, including the boundaries of the UFG and CG regions, are shown in Fig. 7. The concentration of the precipitates (white dots) was remarkably higher in the UFG region compared to that in the CG region.

The volume fractions of the precipitates were 0.6 ± 0.0 %, 1.6 ± 0.1 %, 2.7 ± 0.1 %, and 4.5 ± 0.2 % for samples *d*0.1, *d*0.08, *d*0.06, and *d*0.04, respectively, and significantly increased monotonically with decreasing *d* ($P < 0.05$ by one-way ANOVA) without a significant increase in size for samples *d*0.1–*d*0.06; however, sample *d*0.04 showed an increase in precipitation size due to a significant in situ aging effect. Thus, as shown in Fig. 7(d), the size of the Al_3(Sc, Zr) precipitates of sample *d*0.04 is larger than those of samples *d*0.1–*d*0.06. There are differences in in situ aging with decreasing *d*, resulting in precipitation growth due to a significant remelting of previous scan tracks; however, sample *d*0.06 showed the high volume fraction of UFGs without grain and precipitation growth, showing the importance of the optimization of track-to-track intervals. To further identify the composition, size, and distribution of the precipitates, TEM analysis and TEM-EDS mapping were performed for samples *d*0.1 and *d*0.06.

The HAADF and bright-field images of the UFG region acquired for samples *d*0.1 and *d*0.06 are shown in Fig. 8; clearly, there is no significant precipitation growth, and the average precipitation size is approximately 40 nm for both samples *d*0.1 and *d*0.06. The precipitates were distributed both inside the grains and at grain boundaries, but the populations were higher at grain boundaries. The precipitates located inside the grains, which acted as nucleation sites, and at the grain boundaries, which hampered grain growth, were identified for Scalmalloy samples, corresponding to the findings of Spierings *et al.* [19].

Fig. 9 displays the HAADF-STEM images and corresponding elemental STEM-EDS maps of the UFG region acquired for samples *d*0.1 and *d*0.06, respectively; clearly, the tendency of precipitation composition is similar for both samples, such that Mg, Sc, Zr, Fe, Mn, and Si segregate and the remaining Mg is a solute in the Al matrix. The amount of precipitation was evidently higher in sample *d*0.06 than *d*0.1 owing to the more track–track boundary formation accompanying lower cooling rates owing to higher energy density with the lower *d*. Therefore, the matrix composition of sample *d*0.1 was Al–4.1Mg–0.7Sc–0.3Zr–0.8Mn–0.1Fe–0.01Si–1O and that of sample *d*0.06 was Al–3.3Mg–0.6Sc–0.2Zr–0.8Mn–0.1Fe–0.01Si–0.7O, exhibiting lower solid solution elements compared to *d*0.1 due to the higher precipitation rate, correlating with the precipitation distribution. Further, the Mg concentrations determined using SEM-EDS were 4.1 ± 0.2, 4.0 ± 0.0, 3.4 ± 0.2, and 3.1 ± 0.2 for *d*0.1, *d*0.08, *d*0.06, and *d*0.04, respectively. The Mg concentration significantly decreased with decreasing *d* ($P < 0.05$ by ANOVA), which was consistent with the tendency obtained via TEM-EDS.

According to the aforementioned results, it can be confirmed that sub-micron Al_3(Sc, Zr) precipitates formed in the Al matrix, and that Mg and Si segregations occurred in the grain boundaries. This suggests that Mg_2Si precipitates because Al and Mg_2Si form a eutectic system [31], which is a minor precipitation considering the low amount of Si in Scalmalloy; similarly, the segregations of Fe and Mn at the grain boundaries were detected as shown in Fig. 9.

The Vickers hardness of the samples with different hatch spacing *d* measured in the YZ plane is listed in Table 2. It increased from sample *d*0.1 to sample *d*0.06 but decreased for sample *d*0.04. The maximum Vickers hardness of 132 ± 4 $HV_{0.1}$ was obtained for sample *d*0.06, indicating an optimal volume fraction

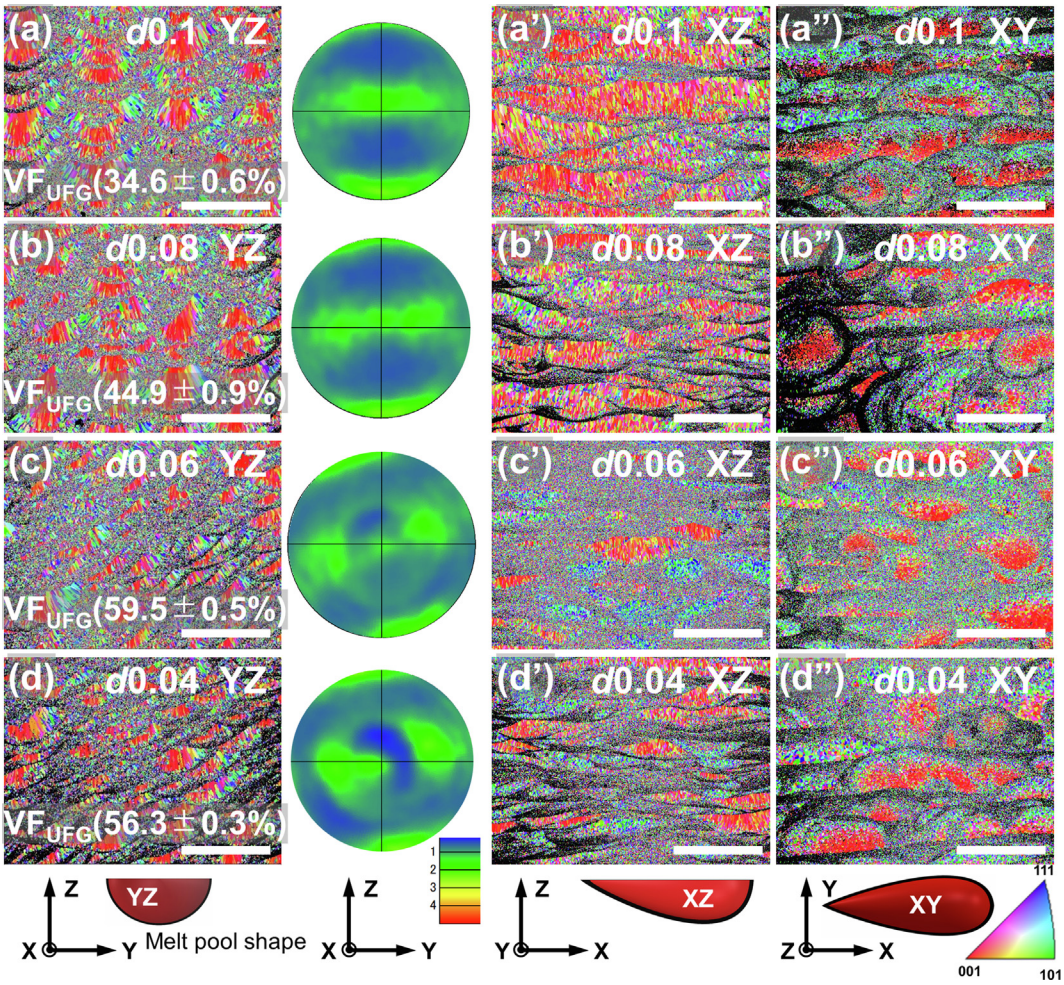

Fig. 5. EBSD inverse pole figure maps and the corresponding {001} pole figures and volume fractions of UFGs inserted, and the schematics of the melt pool shapes recorded in the YZ, XZ, and XY planes. VF_{UFG} is the volume fraction of the UFG region. Scale bars: 200 μm.

of UFG and precipitation size and distribution, which play critical roles in hardness.

Fig. 10(a) shows the tensile nominal stress–strain curves of the samples at room temperature. All samples exhibited typical Portevin–Le Chatelier serrated flow [21], which is often observed in LPBF-fabricated Al-Mg-based alloys. Furthermore, it has been reported that this behavior is caused by the dynamic interactions between Mg atoms and mobile dislocations during deformation [21]. The highest tensile elongation (23.1 % ± 2.5 %) was achieved in sample *d*0.1, in which the CG region is more predominant among the samples. This result is consistent with those of previous studies, which have suggested that the bimodal grain size distribution induces strain hardening and stabilizes tensile deformation, which results in high ductility [32,33]. However, the decrease in elongation with decreasing hatch spacing (Fig. 10(b)) could relate to the increase in the volume fraction of UFGs, as shown in Fig. 5.

The highest ultimate tensile strength (UTS) (415 ± 4 MPa) and yield stress (380 ± 6 MPa) were obtained for sample *d*0.06, which exhibited the highest volume fraction of UFGs; its elongation was lower than that of sample *d*0.1 owing to a lower volume fraction of elongated CGs. As shown in Fig. 10(b) and summarized in Table 2, *d* clearly affects the tensile strength, reaching a value more than twice the tensile strength of casted Scalmalloy, which had an average grain size of 25 μm with agglomerated precipitations [34]. Furthermore, it was observed that the UTS increased with decreasing *d* from 0.1 to 0.06 mm, indicating the activation of multiple strengthening mechanisms due to differences in the volume fraction of UFGs and precipitates; this is discussed in Section 4.3. The maximum yield stress of sample *d*0.06 was 380 MPa, higher than that of sample *d*0.04. The elongation decreased with decreasing *d*, and this tensile strength behavior was attributable to the microstructure of the samples.

4. Discussion

4.1. Pore formation

There are several reasons for pore formation in LPBF-manufactured Al alloys, such as hydrogen porosity [17], a porosity due to light element evaporation such as Mg [35], and porosity due to high *E* input [36].

Hydrogen is a representative gas known to be soluble in liquid aluminum, and its absorption into liquid Al is due to the decomposition of moisture in the air and the oxidation of Al. Therefore, hydrogen porosity is becoming a common problem in the production of Al-alloy.

As shown in Fig. 2, significant spherical pores were present in sample *d*0.04, which had a detrimental effect on densification. Spherical pores are generally formed during the melting process either by the trapping of the protection gas (Ar) or by gases generated upon melting (through which metallic vapor is trapped at rapid cooling rates) [37]. A high *E* causes an unstable melt pool

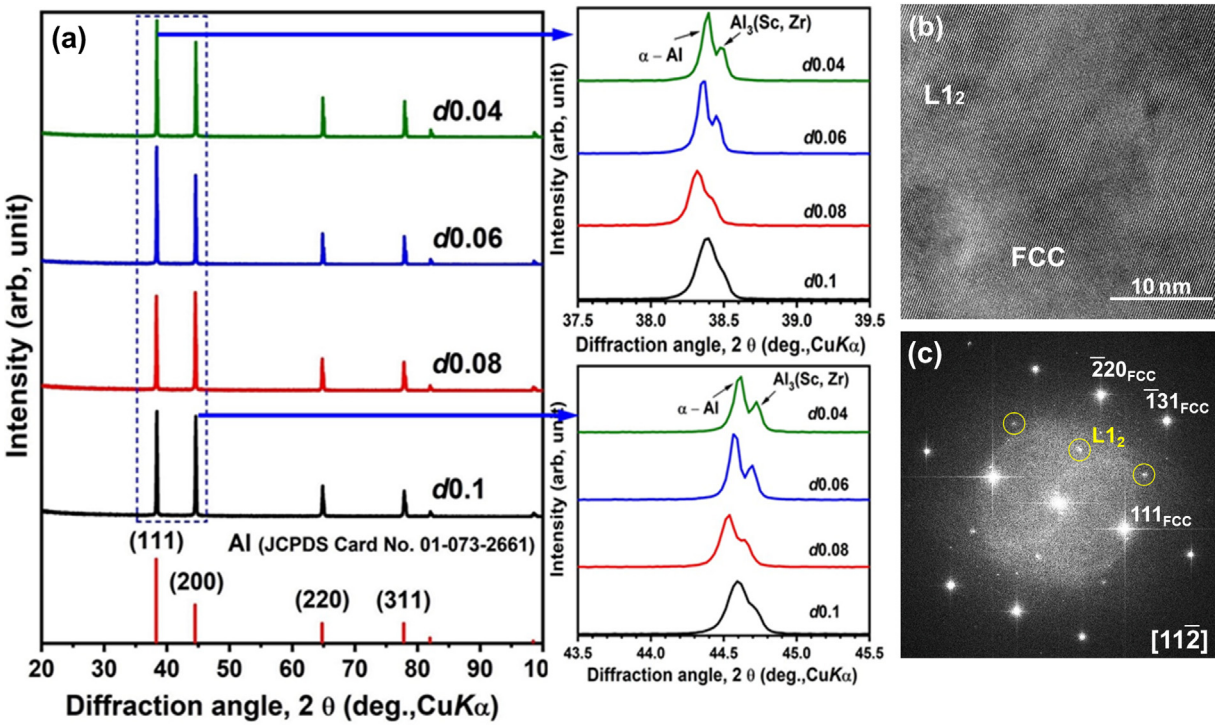

Fig. 6. (a) XRD patterns of the LPBF-fabricated samples, and (b) high-resolution TEM image and (c) fast Fourier transform pattern obtained from the $L1_2$ region.

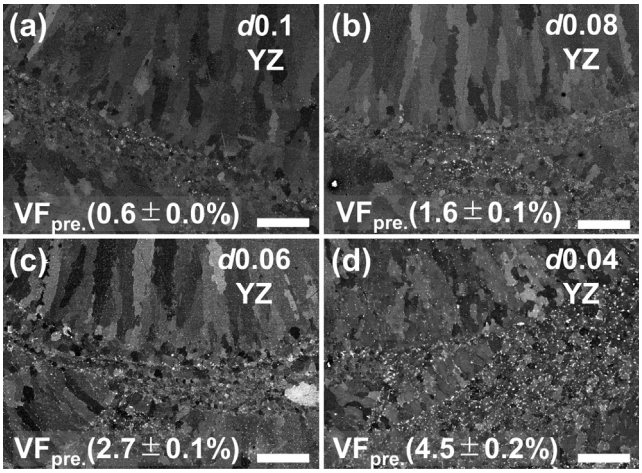

Fig. 7. BSE images of the YZ plane of the samples with the volume fraction, $VF_{pre.}$ of precipitates. Scale bars: 10 μm.

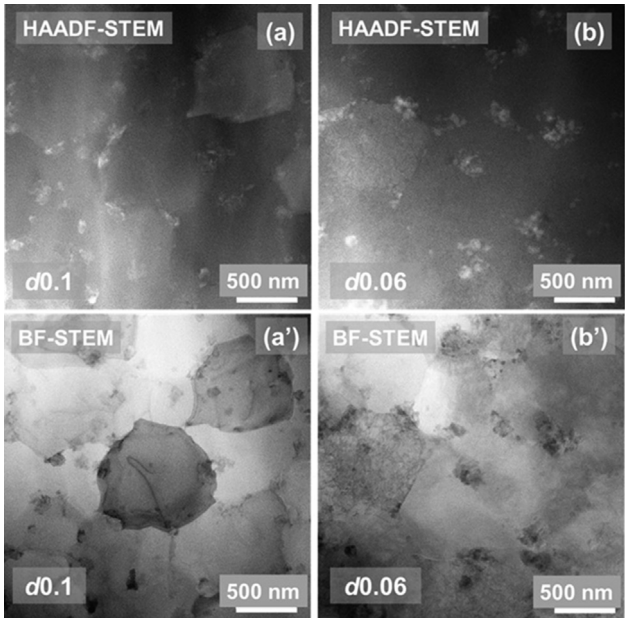

Fig. 8. HAADF and bright-field-STEM images of the UFG region acquired for the as-built samples.

and increases Marangoni convection [36], which leads to increased trapping of the protection gas, thus forming spherical pores. In addition, in this study, the E for sample $d0.04$ was 250 J mm^{-3}, which is only slightly beyond the reported optimal range of E = 77–238 J mm^{-3} [18,19,38], thus exhibiting an unstable melt pool and increased porosity. In addition, SEM-EDS results found that the Mg amount in the samples decreased with decreasing d, indicating that Mg evaporation occurred during the LPBF process.

4.2. Effect of hatch spacing on the microstructure

The smaller d increases the laser spot overlap and remelting zone, resulting in an increase in track–track MPBs, where Al_3(Sc, Zr) precipitates and the nucleation of UFGs occurs. Therefore, in this study, the reduction in d increased both the volume fraction of UFGs and precipitates, as shown in Figs. 5 and 7, respectively. The volume fraction of the UFGs increased without any significant grain growth owing to the presence of sufficient high grain-restricting factors [31]. Large amounts of precipitates at the grain boundaries from potent nucleates, as shown in Figs. 7, 8 and 9, and high cooling rates of the LPBF process all contributed to preventing grain growth and helping the formation of UFGs. This behavior was consistent with that reported in previous studies that investigated the effects of heat treatment on the microstructure and mechanical properties of Scalmalloy [25]. Li *et al.* [25] found

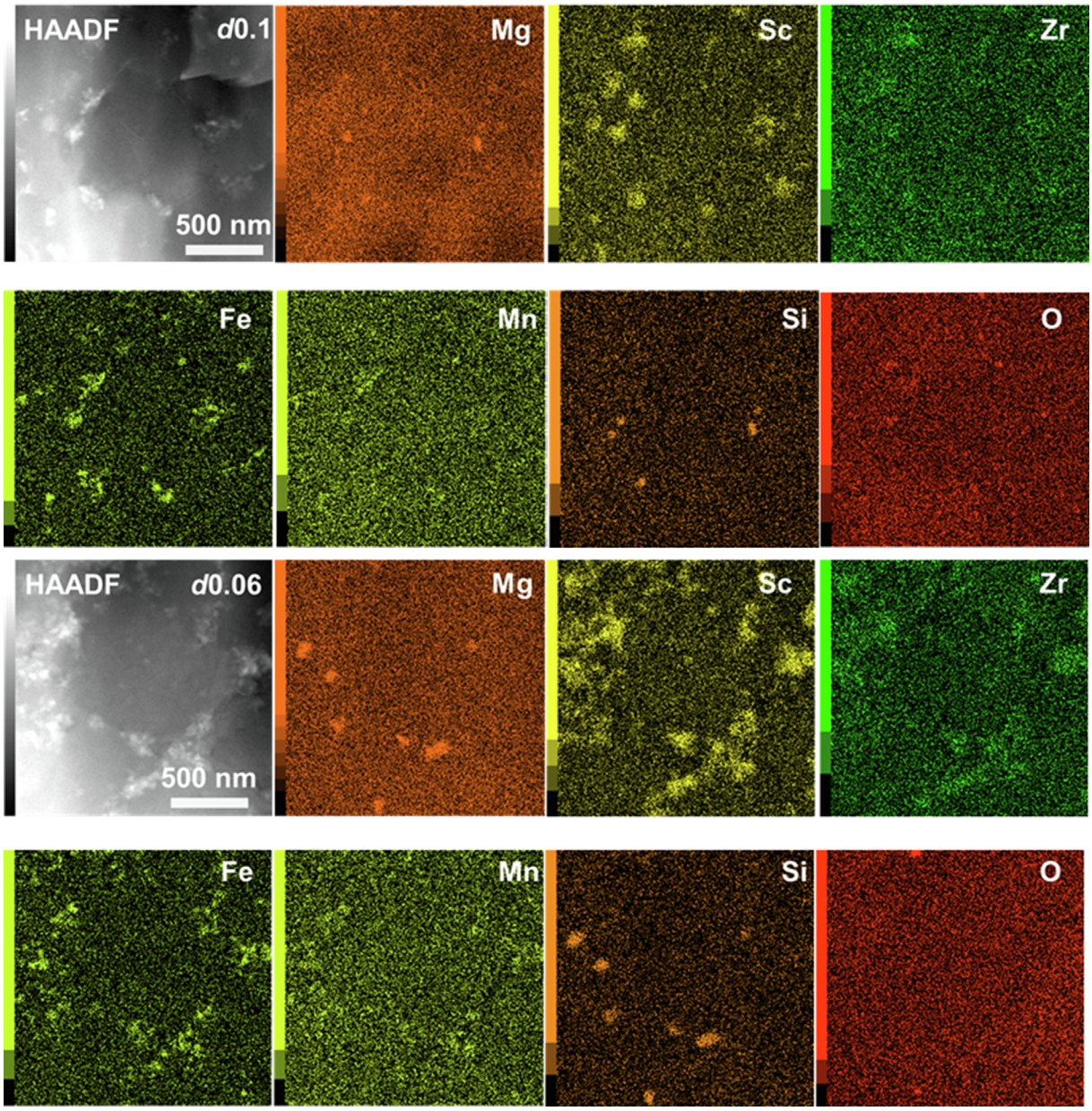

Fig. 9. HAADF-STEM images and elemental STEM-EDS maps of the UFG region acquired for samples *d*0.1 and *d*0.06.

that the change in grain size was not distinct before and after aging treatment at 300–350 °C for 4–12 h because of the inhibition of grain growth by the nanoscale Al_3(Sc, Zr) precipitates at the grain boundaries. Although a decreasing *d* is expected to induce an intrinsic in situ aging effect, the average UFG sizes exhibited insignificant differences with decreasing *d*, which were 1.48, 1.26, 1.05, and 1.08 μm for samples *d*0.1, *d*0.08, *d*0.06, and *d*0.04, respectively. However, the volume fraction of the precipitates increased without size increment for samples *d*0.1–*d*0.06, as shown in Fig. 7, which resulted in an increase in the volume fraction of UFGs. It has been reported that there are two types of Al_3(Sc, Zr) precipitation mechanisms during LPBF [19,39]. One is formed during the solidification process located at the MPBs, which can act as a nucleation site to promote UFGs and improve hot-tear resistance. The other is formed during the intrinsic aging process, which contributes to precipitate strengthening and further enhances the mechanical strength [40]. The smaller *d* increased the track–track MPBs due to laser spot overlapping and led to an increased volume fraction of precipitates and a subsequent increase in the volume fraction of UFGs. However, a slight precipitate size increment occurred when *d* was 0.04 mm, as shown in Fig. 7. This is because a small *d* produces a high *E*, which increases the temperature of the melt pool and promotes the periodic heat effect on the previous molten regions [41]. Thus, the in situ aging effects became more noticeable and led to increments in the precipitation size, indicating the importance of adjusting track-to-track intervals to control the bimodal microstructure.

As shown in Fig. 11, the dislocation density of sample *d*0.06 was much higher than that of *d*0.1. It is assumed that these dislocations were mainly generated by residual stress, as mentioned in Fig. 6 in the XRD pattern. The peaks of sample *d*0.06 shifted to the low-angle side compared to *d*0.1, which implied the accumulation of residual stress in sample *d*0.06, consistent with the results of a previous study [25]. The above investigations demonstrated that the optimal *d* (*d*0.06 in this study) for Scalmalloy LPBF processing exhibited an increase in the volume fraction of precipitation and

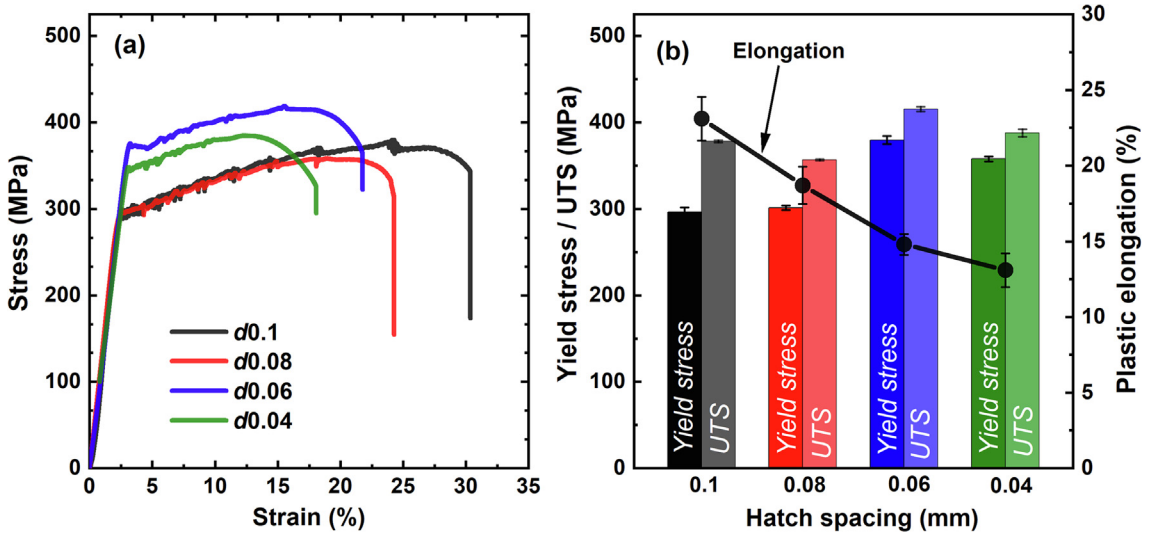

Fig. 10. (a) Tensile stress–strain curves and (b) yield stress, ultimate tensile strength (UTS), and elongation of each sample.

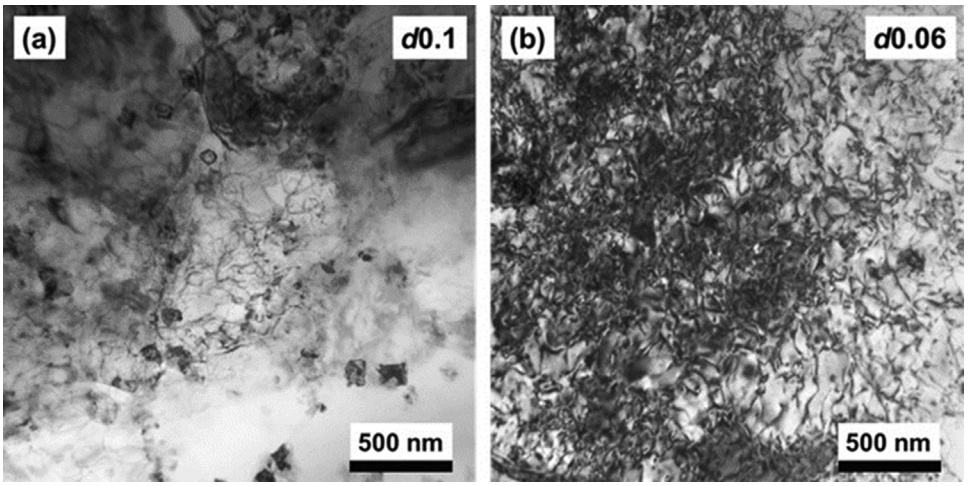

Fig. 11. Dislocation structure of the UFG regions.

UFG while exhibiting higher dislocation density. Thus, the promotion of track–track MPBs presented in this study was effective in tuning the microstructure of Scalmalloy to enhance the mechanical properties.

The strategy to increase the volume fraction of UFG for Scalmalloy is aimed at increasing/optimizing precipitates, and the precipitation process depends on temperature and time. Thus, it is dependent on the cooling rates associated with laser scan parameters. Spierings *et al.* [19] investigated the relationships between the precipitates and laser scan speed and found that the samples manufactured with higher laser scan speed included fewer precipitates than that of the sample manufactured with lower laser scan speed. Further, they demonstrated that it is caused by the high cooling rates at higher laser scan speeds. Therefore, decreasing cooling rates, meaning increasing *E*, increases precipitates and leads to more UFG formation. In this study, we used a similar approach, decreasing *d* equivalent to increasing *E*, and, as shown in Figs. 7 and 5, the volume fraction of precipitates increased, as did the volume fraction of UFG.

Another similar approach that increases the volume fraction of UFG is using high *E* with increasing platform temperature. Yang *et al.* [21] demonstrated that equiaxed grains increase when the platform temperature increases from 35 to 200 °C, and explained that the combination of remelting zone volumes and decreasing thermal gradient promotes precipitates. As described above, decreasing cooling via increasing *E* indeed promoted precipitates and led to an increased UFG volume fraction. Our approach in this study of decreasing *d* is correlated with these studies. As shown in Fig. 7, the volume fraction of precipitates increased with decreasing *d*, which promoted more UFG formation up to d0.06, as shown in Fig. 5.

4.3. Strengthening mechanisms in LPBF-fabricated Scalmalloy

There are four main strengthening mechanisms in polycrystalline materials, namely solid solution, grain boundary, precipitation, and dislocation strengthening. As the four mechanisms are affected independently, the yield strength is a simple summation of the four individual contributions and can be expressed as [42,43]: $\sigma_y = \sigma_A + \sigma_S + \sigma_G + \sigma_P + \sigma_D$ (1), where σ_A is the yield stress of pure Al (60 MPa) [62], which represents the intrinsic strength or the so-called lattice friction strength, and σ_S [22], σ_G [22], σ_P [44], and σ_D [44] are the strengthening contributions from the solid solution, grain boundary (Hall–Petch), precipitates (Orowan), and

dislocations, respectively. Decreasing d (from 0.1 to 0.06 mm) resulted in an increase in track–track MPBs and promoted precipitation, which led to the nucleation of more UFGs. Thus, a decrease in d resulted in an increase in UFG and precipitation-activated multiple strengthening mechanisms. In this study, σ_S, σ_G, σ_P, and σ_D were calculated and compared with the experimental data. All related equations, parameters, and values from the comparison of the experimental and calculated results are listed in Table 3. The error in the calculated yield stress was derived using the following error propagation function: $\delta\sigma_y = \{(\delta\sigma_A)^2 + (\delta\sigma_S)^2 + (\delta\sigma_G)^2 + (\delta\sigma_P)^2 + (\delta\sigma_D)^2\}^{1/2}$, where $\delta\sigma_i$ is the error of σ_i.

Mg plays a solid solution strengthening role in Scalmalloy, which increases the Al matrix lattice parameter, leading to an increase in precipitation and Al matrix coherence [22]. The Mg solute concentrations $c_{d0.1}$ = 4.1 ± 0.2 wt% and $c_{d0.06}$ = 3.3 ± 0.2 wt % were obtained from STEM-EDS analysis, as described in the Results section. The Mg solute concentration was lower in sample d0.06 than in d0.1, because Mg precipitated more significantly in sample d0.06 owing to the noticeable in situ aging effects of the smaller d, as shown in Fig. 9. According to these Mg solute concentrations, σ_S was calculated based on Eqn. (2) and was 93 ± 1 MPa for sample d0.1 and 84 ± 2 MPa for sample d0.06, as listed in Table 3. These values match well with those reported in a previous study that predicted σ_S increment as a function of the Mg solute content [22]. Kendig *et al.* [23] conducted strengthening mechanism model predictions for Al–Mg–Sc–Zr alloy and reported that the solid solution strengthening is 75–100 MPa when the Mg solute content is 3–5 %. Our calculated results are consistent with those values.

It was determined from the EBSD grain map data that the average UFG grain size was 1.48 μm for sample d0.1 and 1.05 μm for sample d0.06, whereas the average size of CGs was 4.8 μm for sample d0.1 and 3.1 μm for sample d0.06. A smaller d has a stronger in situ aging effect than that of a larger d [41]; however, grain growth did not occur in the smaller d sample owing to the promotion of precipitation formation. The effect of σ_G on the material strength can be determined based on the Hall–Petch relationship, as shown in Eq. (3) in Table 3. According to the Hall–Petch relationship, smaller grains exhibit a higher σ_G, because finer grains generate more grain boundaries per unit volume. Using this equation, the average σ_G in this study was calculated as 100 ± 4 MPa for sample d0.1 and 131 ± 6 MPa for sample d0.06.

Precipitate strengthening occurs through a dislocation bypass (Orowan-type) or particle shearing mechanism. Generally, the Orowan mechanism occurs when the particle radius exceeds a critical value, whereas the shearing mechanism dominates when the precipitates are sufficiently small and coherent [43,45]. The critical radius at which the deformation mechanism changes from precipitate shearing to an Orowan bypass mechanism in the Al–Sc system ranges from 1.5 to 2.0 nm [45,46]. In this study, the average precipitate radius was 40 nm, exceeding the critical value range of 1.5–2.0 nm; therefore, the Orowan bypass mechanism is expected to be operative. Precipitate strengthening σ_P was calculated based on Eq. (4) in Table 3. From TEM observation, it was found that the average precipitation radius $< R >$ was the same for both samples (∼40 nm), while the volume fractions of precipitates ϕ were $\phi_{d0.1}$ = 0.6 ± 0.0 % and $\phi_{d0.06}$ = 2.7 ± 0.1 %, obtained from BSE observations. According to these data, the values of σ_P were calculated based on Eqs. (4) and (5) in Table 3 as σ_P = 23 ± 0 MPa for sample d0.1 and 54 ± 0 MPa for sample d0.06. As Spierings *et al.* [19] reported, the increasing E via decreasing laser scan speed increased mechanical properties such as YS and UTS, primarily because of the increasing strengthening of the precipitates. Their results are congruent with those obtained in this study.

The plastic deformation results from the movement of mobile dislocations and the strengthening by dislocations were calculated based on Eq. (6) in Table 3. As shown in Fig. 11, sample d0.06 showed a higher ρ_{dis} than that of d0.1, owing to the higher residual stress in the smaller d sample. Here, ρ_{dis} was estimated using the Williamson–Hall method, a widely used method to assess the effects of microstrain and crystallite size [43,47]. In this approach, XRD peak broadening β includes crystallite size broadening β_G and strain broadening β_S [48,49], as shown below:

$$\beta = \beta_G + \beta_S \tag{7}$$

$$\beta_G = K\lambda/(D\cos\theta) \tag{8}$$

$$\beta_S = 4\varepsilon\tan\theta \tag{9}$$

where K = 0.9 is a constant, λ = 0.15405 nm is the wavelength of Cu Kα radiation, D is the crystallite size, ε is the microstrain, and θ is the Bragg angle of the peak. β and θ can be obtained by fitting the XRD peaks. Focusing on the microstrain ε only, Eq. (7) can be rewritten as:

$$\beta\cos\theta = K\lambda/D + (4\sin\theta)\varepsilon \tag{10}$$

Table 3
Equations and input parameters for the calculation of yield stress for samples d0.1 and d0.06.

Strengthening mechanisms	Parameters	Calc. yield stress (MPa)	
		d0.1	d0.06
Intrinsic strengthening σ_A		60	60
Solid solution strengthening $\sigma_S = \frac{3.1\varepsilon G c^{1/2}}{700}$ (2)	ε = 3.8 × 10^{-7} (experimental constant) G = 26 GPa (shear modulus of the matrix) c (concentration of the solute) $c_{d0.1}$ = 4.1 ± 0.2 wt%; $c_{d0.06}$ = 3.3 ± 0.2 wt%	93 ± 1	84 ± 2
Grain boundary strengthening $\sigma_G = k_d^{1/2}$ (3)	k = 0.17 MN/$m^{3/2}$ (strengthening coefficient) $d_{0.1UFG}$ = 1.48 ± 0.16 μm; $d_{0.06UFG}$ = 1.05 ± 0.14 μm $d_{0.1CG}$ = 4.8 ± 0.2 μm; $d_{0.06CG}$ = 3.1 ± 0.1 μm (average grain size)	100 ± 4	131 ± 6
Precipitation strengthening $\sigma_{orowan} = M\frac{0.4}{\pi}\frac{Gb}{\sqrt{1-\nu}}\frac{\ln\left(\frac{\sqrt{2/3}\langle R\rangle}{b}\right)}{\lambda}$ (4) $\lambda = \left[\left(\frac{3\pi}{4\phi}\right)^{\frac{1}{2}} - 1.64\right]\langle R\rangle$ (5)	M = 3.06 (Taylor factor) $<R>$ = 40 ± 1 nm (radius of the particles) $\phi_{d0.1}$ = 0.6 ± 0.0 %; $\phi_{d0.06}$ = 2.7 ± 0.0 % (volume fraction of particles) λ (inter-particle spacing) b = 0.248 nm (Burger's vector) ν = 0.34 (Poisson's ratio for Al)	23 ± 0	54 ± 0
Dislocation strengthening $\sigma_D = M\alpha Gb\rho^{1/2}$ (6)	α = 0.2 (constant) $\rho_{d0.1}$ = 1.49 ± 0.12 × 10^{13} m^{-2}; $\rho_{d0.06}$ = 4.92 ± 0.13 × 10^{13} m^{-2} (dislocation density)	17 ± 1	32 ± 0
	Calculated yield stress	294 ± 4	360 ± 6
	Experimental yield stress	296 ± 9	380 ± 6

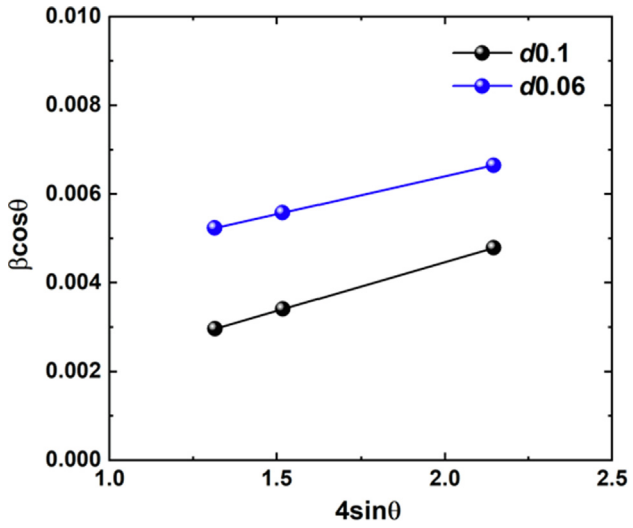

Fig. 12. Line-fitted peak broadening β as a function of 4tanθ. The slope of the fitted line represents the value of microstrain ε.

As shown in Fig. 12, the linear fit of the $\beta\cos\theta$–$4\sin\theta$ plot determines D and ε, and the dislocation density can then be calculated from the equation below [50,51]:

$$\rho_{dis} = 2\sqrt{3}\varepsilon/(Db)x \quad (11)$$

ρ_{dis}, calculated using Eq. (10), was 1.49×10^{13} m^{-2} for sample d0.1 and 4.92×10^{13} m^{-2} for sample d0.06. Accordingly, σ_D was calculated based on Eq. (6) in Table 3 and was 17 ± 1 MPa for sample d0.1 and 32 ± 0 MPa for sample d0.06.

As shown in Fig. 13, the order of contributors to the alloy strength was $\sigma_G > \sigma_S > \sigma_P > \sigma_D$ for both samples d0.1 and d0.06. This is consistent with the results of a previous study [22], thus supporting the validity of the approach adopted in this study to promote UFGs with track–track MPBs. It can be observed that the largest difference in YS between samples d0.1 and d0.06 results from the difference in σ_P and σ_D. The σ_P and σ_D of sample d0.06 are approximately twice those of sample d0.1. Therefore, the main difference in YS for these two samples is attributable to the significant difference in σ_P and σ_D. The σ_P difference observed between the smaller and larger d samples is attributable to the small d samples promoting precipitation formation by increasing MPBs and simultaneously promoting precipitation formation through the in situ aging effect [41].

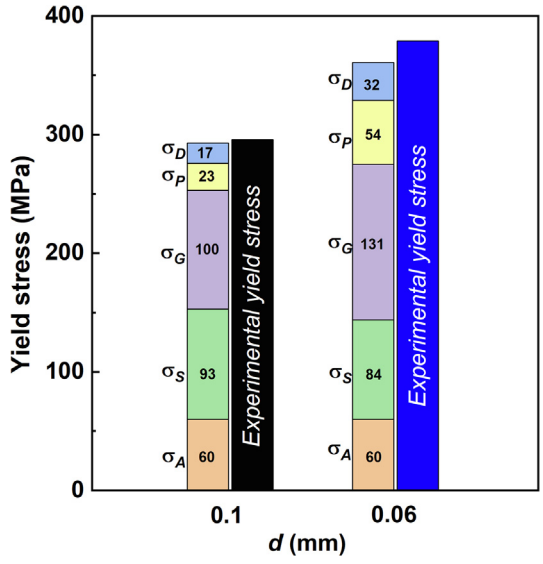

Fig. 13. Comparison between the calculated and experimentally obtained yield stress. Contributions summed from solid solution strengthening σ_S, grain boundary strengthening σ_G, precipitation strengthening σ_P, and dislocation strengthening σ_D.

The tensile strength increased with a decrease in d from 0.1 to 0.06 mm; however, it decreased for sample d0.04, as shown in Fig. 10. This decrease in tensile strength may be due to sample d0.04 exhibiting the highest porosity among all samples owing to the high E input causing gas trapping phenomena. The pores in sample d0.04 were determined to be gas pores, and it was reported that the gas pores form a spherical morphology with pore diameters ranging from 10 to 130 μm [52]. These spherical pores have no detrimental effects on the mechanical properties [53]. However, the size of the pores of sample d0.04 slightly exceeded the range of 10–130 μm; therefore, it can be expected that the porosity of sample d0.04 resulted in the degraded mechanical properties.

This study is believed to be the first report on optimizing strength and ductility by decreasing d and promoting track–track MPBs to increase precipitation and consequent UFG formation. The effects of d on the mechanical properties were significant, considering the microstructural behaviors and strengthening mechanisms. The Scalmalloy samples in this study satisfied the mechanical requirements for cast Scalmalloy [28] by microstructural control through the optimization of d.

5. Conclusions

The effects of the laser hatch spacing, d, on the densification, microstructure, and mechanical properties of Scalmalloy were systematically investigated, and the optimum processing range was established for enhanced strength and ductility. The following conclusions are drawn from this study:

(1) The SCALMA40B5 alloy exhibits good processability with LPBF over a wide hatch spacing range of 0.06–0.1 mm, which is associated with a laser energy density range of 100–166 J/mm^3.
(2) The relative density of the materials produced within such a range is above 99.5 %. The majority of the pores detected using the established processing parameters were relatively spherical with regular geometry. There were no cracks or lack-of-fusion pores.
(3) The microstructure of the as-fabricated material involves a unique bimodal grain structure. The UFG region with no preferential crystallographic orientation constitutes the melt pool boundary, whereas CGs prevail in the melt pool center, preferentially growing along the thermal gradient direction. The anisotropic microstructure formed by d0.1 is diminished by decreasing the hatch space.
(4) The mechanical properties of as-fabricated samples show an excellent combination of strength and ductility. The alloy has a maximum yield strength of 380 ± 6 MPa with a 14.8 ± 1.2 % elongation at a laser hatch spacing of 0.06 mm.
(5) Grain boundary strengthening is the largest contributor, with solid solution and precipitate strengthening also making substantial contributions; in addition, dislocation strengthening significantly increases with decreasing d.

This study demonstrated a successful method for effectively strengthening Scalmalloy by adjusting the LPBF process parameters. Consequently, a smaller d increased track-by-track MPBs and promoted precipitation and UFG formation, which promoted multiple strengthening mechanisms. These findings can provide

opportunities for the future development of alloys for high-temperature structural applications using in situ precipitation strengthening.

Declaration of Competing Interest

The authors declare that they have no known competing financial interests or personal relationships that could have appeared to influence the work reported in this paper.

Acknowledgements

This work was supported by a Grant-in-Aid for Scientific Research (JP18H05254) from the Japan Society for the Promotion of Science (JSPS) and CREST - Nanomechanics: Elucidation of macroscale mechanical properties based on understanding nanoscale dynamics for innovative mechanical materials (Grant Number: JPMJCR2194) from the Japan Science and Technology Agency (JST).

Data availability

The datasets used and analyzed during the current study are available from the corresponding author on reasonable request.

Appendix A. Supplementary material

Supplementary data to this article can be found online at https://doi.org/10.1016/j.matdes.2022.110976.

References

[1] T.S. Srivatsan, T.S. Sudarshan, Additive Manufacturing: Innovations, Advances, and Applications, CRC Press, 2015.
[2] J.P. Davim, Lasers in Manufacturing, WILEY (2012).
[3] J.P. Davim, Modern Mechanical Engineering, Springer, 2014.
[4] O. Gokcekaya, T. Ishimoto, S. Hibino, J. Yasutomi, T. Narushima, T. Nakano, Unique crystallographic texture formation in Inconel 718 by laser powder bed fusion and its effect on mechanical anisotropy, Acta Mater. 212 (2021), https://doi.org/10.1016/j.actamat.2021.116876 116876.
[5] O. Gokcekaya, T. Ishimoto, T. Todo, R. Suganuma, R. Fukushima, T. Narushima, T. Nakano, Effect of scan length on densification and crystallographic texture formation of pure chromium fabricated by laser powder bed fusion, Crystals 11 (2020) 9, https://doi.org/10.3390/cryst11010009.
[6] C. Zhao, Y. Bai, Y. Zhang, X. Wang, J.M. Xue, H. Wang, Influence of scanning strategy and building direction on microstructure and corrosion behaviour of selective laser melted 316L stainless steel, Mater. Des. 209 (2021), https://doi.org/10.1016/j.matdes.2021.109999 109999.
[7] S.-H. Sun, T. Ishimoto, K. Hagihara, Y. Tsutsumi, T. Hanawa, T. Nakano, Excellent mechanical and corrosion properties of austenitic stainless steel with a unique crystallographic lamellar microstructure via selective laser melting, Scr. Mater. 159 (2019) 89–93, https://doi.org/10.1016/j.scriptamat.2018.09.017.
[8] Y. Tsutsumi, T. Ishimoto, T. Oishi, T. Manaka, P. Chen, M. Ashida, K. Doi, H. Katayama, T. Hanawa, T. Nakano, Crystallographic texture- and grain boundary density-independent improvement of corrosion resistance in austenitic 316L stainless steel fabricated via laser powder bed fusion, Addit. Manuf. 45 (2021), https://doi.org/10.1016/j.addma.2021.102066 102066.
[9] A. Takase, T. Ishimoto, R. Suganuma, T. Nakano, Surface residual stress and phase stability in unstable β-type Ti–15Mo–5Zr–3Al alloy manufactured by laser and electron beam powder bed fusion technologies, Addit. Manuf. 47 (2021), https://doi.org/10.1016/j.addma.2021.102257.
[10] T. Ishimoto, K. Hagihara, K. Hisamoto, S.-H. Sun, T. Nakano, Crystallographic texture control of beta-type Ti–15Mo–5Zr–3Al alloy by selective laser melting for the development of novel implants with a biocompatible low Young's modulus, Scr. Mater. 132 (2017) 34–38, https://doi.org/10.1016/j.scriptamat.2016.12.038.
[11] H. Jia, Q. Song, R. Wang, W. Cai, Z. Liu, Evaluation and prediction of pore effects on single-crystal mechanical and damage properties of selective laser melted Inconel-718, Mater. Des. 219 (2022), https://doi.org/10.1016/j.matdes.2022.110807 110807.
[12] S. Hibino, T. Todo, T. Ishimoto, O. Gokcekaya, Y. Koizumi, K. Igashira, T. Nakano, Control of crystallographic texture and mechanical properties of Hastelloy-X via laser powder bed fusion, Crystals 11 (2021), https://doi.org/10.3390/cryst11091064.
[13] P.A. Rometsch, Y. Zhu, X. Wu, A. Huang, Review of high-strength aluminium alloys for additive manufacturing by laser powder bed fusion, Mater. Des. 219 (2022), https://doi.org/10.1016/j.matdes.2022.110779 110779.
[14] Y. Geng, Q. Wang, Y. Wang, Q. Zang, S. Mi, J. Xu, Y. Xiao, Y. Wu, J. Luan, Microstructural evolution and strengthening mechanism of high-strength AlSi8.1 Mg1.4 alloy produced by selective laser melting, Mater. Des. 218 (2022) 110674, https://doi.org/10.1016/j.matdes.2022.110674.
[15] T. Kimura, T. Nakamoto, Microstructures and mechanical properties of A356 (AlSi7Mg0.3) aluminum alloy fabricated by selective laser melting, Mater. Des. 89 (2016) 1294–1301, https://doi.org/10.1016/j.matdes.2015.10.065.
[16] J. Gheysen, M. Marteleur, C. van der Rest, A. Simar, Efficient optimization methodology for laser powder bed fusion parameters to manufacture dense and mechanically sound parts validated on AlSi12 alloy, Mater. Des. 199 (2021), https://doi.org/10.1016/j.matdes.2020.109433 109433.
[17] C. Weingarten, D. Buchbinder, N. Pirch, W. Meiners, K. Wissenbach, R. Poprawe, Formation and reduction of hydrogen porosity during selective laser melting of AlSi10Mg, J. Mater. Process. Technol. 221 (2015) 112–120, https://doi.org/10.1016/j.jmatprotec.2015.02.013.
[18] A.B. Spierings, K. Dawson, P.J. Uggowitzer, K. Wegener, Influence of SLM scan-speed on microstructure, precipitation of Al3Sc particles and mechanical properties in Sc- and Zr-modified Al-Mg alloys, Mater. Des. 140 (2018) 134–143, https://doi.org/10.1016/j.matdes.2017.11.053.
[19] A.B. Spierings, K. Dawson, T. Heeling, P.J. Uggowitzer, R. Schäublin, F. Palm, K. Wegener, Microstructural features of Sc- and Zr-modified Al-Mg alloys processed by selective laser melting, Mater. Des. 115 (2017) 52–63, https://doi.org/10.1016/j.matdes.2016.11.040.
[20] K.V. Yang, Y. Shi, F. Palm, X. Wu, P. Rometsch, Columnar to equiaxed transition in Al-Mg(-Sc)-Zr alloys produced by selective laser melting, Scr. Mater. 145 (2018) 113–117, https://doi.org/10.1016/j.scriptamat.2017.10.021.
[21] A.B. Spierings, K. Dawson, K. Kern, F. Palm, K. Wegener, SLM-processed Sc- and Zr- modified Al-Mg alloy: Mechanical properties and microstructural effects of heat treatment, Mater. Sci. Eng., A 701 (2017) 264–273, https://doi.org/10.1016/j.msea.2017.06.089.
[22] K.L. Kendig, D.B. Miracle, Strengthening mechanisms of an Al-Mg-Sc-Zr alloy, Acta Mater. 50 (2002) 4165, https://doi.org/10.1016/S1359-6454(02)00258-6.
[23] W. Shifeng, L. Shuai, W. Qingsong, C. Yan, Z. Sheng, S. Yusheng, Effect of molten pool boundaries on the mechanical properties of selective laser melting parts, J. Mater. Process. Technol. 214 (2014) 2660–2667, https://doi.org/10.1016/j.jmatprotec.2014.06.002.
[24] D. Gu, H. Zhang, D. Dai, C. Ma, H. Zhang, Y. Li, S. Li, Anisotropic corrosion behavior of Sc and Zr modified Al-Mg alloy produced by selective laser melting, Corros. Sci. 170 (2020), https://doi.org/10.1016/j.corsci.2020.108657.
[25] R. Li, H. Chen, H. Zhu, M. Wang, C. Chen, T. Yuan, Effect of aging treatment on the microstructure and mechanical properties of Al-3.02Mg-0.2Sc-0.1Zr alloy printed by selective laser melting, Mater. Des. 168 (2019) 107668, https://doi.org/10.1016/j.matdes.2019.107668.
[26] J. Ma, B. Franco, G. Tapia, K. Karayagiz, L. Johnson, J. Liu, R. Arroyave, I. Karaman, A. Elwany, Spatial control of functional response in 4D-printed active metallic structures, Sci. Rep. 7 (2017) 46707, https://doi.org/10.1038/srep46707.
[27] D. Gu, Y. Shen, Effects of processing parameters on consolidation and microstructure of W-Cu components by DMLS, J. Alloys Compd. 473 (1–2) (2009) 107–115, https://doi.org/10.1016/j.jallcom.2008.05.065.
[28] O. Gokcekaya, N. Hayashi, T. Ishimoto, K. Ueda, T. Narushima, T. Nakano, Crystallographic orientation control of pure chromium via laser powder bed fusion and improved high temperature oxidation resistance, Addit. Manuf. 36 (2020), https://doi.org/10.1016/j.addma.2020.101624 101624.
[29] C. Pleass, S. Jothi, Influence of powder characteristics and additive manufacturing process parameters on the microstructure and mechanical behaviour of Inconel 625 fabricated by Selective Laser Melting, Addit. Manuf. 24 (2018) 419–431, https://doi.org/10.1016/j.addma.2018.09.023.
[30] L. Wang, X. Jiang, Y. Zhu, X. Zhu, J. Sun, B. Yan, An approach to predict the residual stress and distortion during the selective laser melting of AlSi10Mg parts, Int. J. Adv. Manuf. Technol. 97 (2018) 3535–3546, https://doi.org/10.1007/s00170-018-2207-3.
[31] R. Li, M. Wang, Z. Li, P. Cao, T. Yuan, H. Zhu, Developing a high-strength Al-Mg-Si-Sc-Zr alloy for selective laser melting: Crack-inhibiting and multiple strengthening mechanisms, Acta Mater. 193 (2020) 83–98, https://doi.org/10.1016/j.actamat.2020.03.060.
[32] J.R. Croteau, S. Griffiths, M.D. Rossell, C. Leinenbach, C. Kenel, V. Jansen, D.N. Seidman, D.C. Dunand, N.Q. Vo, Microstructure and mechanical properties of Al-Mg-Zr alloys processed by selective laser melting, Acta Mater. 153 (2018) 35–44, https://doi.org/10.1016/j.actamat.2018.04.053.
[33] D. Witkin, Z. Lee, R. Rodriguez, S. Nutt, E. Lavernia, Al–Mg alloy engineered with bimodal grain size for high strength and increased ductility, Scr. Mater. 49 (2003) 297–302, https://doi.org/10.1016/s1359-6462(03)00283-5.
[34] M. Wang, R. Li, T. Yuan, C. Chen, L. Zhou, H. Chen, M. Zhang, S. Xie, Microstructures and mechanical property of AlMgScZrMn - A comparison between selective laser melting, spark plasma sintering and cast, Mater. Sci. Eng., A 756 (2019) 707 354-364, https://doi.org/10.1016/j.msea.2019.04.060.
[35] H. Rao, S. Giet, K. Yang, X. Wu, C.H.J. Davies, The influence of processing parameters on aluminium alloy A357 manufactured by Selective Laser Melting, Mater. Des. 109 (2016) 334–346, https://doi.org/10.1016/j.matdes.2016.07.009.

[36] M. Rombouts, J.P. Kruth, L. Froyen, P. Mercelis, Fundamentals of Selective Laser Melting of alloyed steel powders, CIRP Ann. 55 (2006) 187–192, https://doi.org/10.1016/s0007-8506(07)60395-3.
[37] K. Moussaoui, W. Rubio, M. Mousseigne, T. Sultan, F. Rezai, Effects of Selective Laser Melting additive manufacturing parameters of Inconel 718 on porosity, microstructure and mechanical properties, Mater. Sci. Eng., A 735 (2018) 182–190, https://doi.org/10.1016/j.msea.2018.08.037.
[38] A.B. Spierings, K. Dawson, P. Dumitraschkewitz, S. Pogatscher, K. Wegener, Microstructure characterization of SLM-processed Al-Mg-Sc-Zr alloy in the heat treated and HIPed condition, Addit. Manuf. 20 (2018) 173–181, https://doi.org/10.1016/j.addma.2017.12.011.
[39] Y. Shi, P. Rometsch, K. Yang, F. Palm, X. Wu, Characterisation of a novel Sc and Zr modified Al–Mg alloy fabricated by selective laser melting, Mater. Lett. 196 (2017) 347–350, https://doi.org/10.1016/j.matlet.2017.03.089.
[40] Z. Wang, X. Lin, N. Kang, Y. Hu, J. Chen, W. Huang, Strength-ductility synergy of selective laser melted Al-Mg-Sc-Zr alloy with a heterogeneous grain structure, Addit. Manuf. 34 (2020), https://doi.org/10.1016/j.addma.2020.101260 101260.
[41] M.A. Pekok, R. Setchi, M. Ryan, Q. Han, D. Gu, Effect of process parameters on the microstructure and mechanical properties of AA2024 fabricated using selective laser melting, Int. J. Adv. Manuf. Technol. 17 (2020), https://doi.org/10.1007/s00170-020-06346-y.
[42] N. Kamikawa, K. Sato, G. Miyamoto, M. Murayama, N. Sekido, K. Tsuzaki, T. Furuhara, Stress–strain behavior of ferrite and bainite with nano-precipitation in low carbon steels, Acta Mater. 83 (2015) 383–396, https://doi.org/10.1016/j.actamat.2014.10.010.
[43] J.Y. He, H. Wang, H.L. Huang, X.D. Xu, M.W. Chen, Y. Wu, X.J. Liu, T.G. Nieh, K. An, Z.P. Lu, A precipitation-hardened high-entropy alloy with outstanding tensile properties, Acta Mater. 102 (2016) 187–196, https://doi.org/10.1016/j.actamat.2015.08.076.
[44] N.Q. Vo, D.C. Dunand, D.N. Seidman, Atom probe tomographic study of a friction-stir-processed Al–Mg–Sc alloy, Acta Mater. 60 (2012) 7078–7089, https://doi.org/10.1016/j.actamat.2012.09.015.
[45] C. Booth-Morrison, D.C. Dunand, D.N. Seidman, Coarsening resistance at 400°C of precipitation-strengthened Al–Zr–Sc–Er alloys, Acta Mater. 59 (2011) 7029–7042, https://doi.org/10.1016/j.actamat.2011.07.057.
[46] D.N. Seidman, E.A. Marquis, D.C. Dunand, Precipitation strengthening at ambient and elevated temperatures of heat-treatable Al(Sc) alloys, Acta Mater. 50 (2002) 4021–4035, https://doi.org/10.1016/S1359-6454(02)00201-X.
[47] W.H.H.G.K. Williamson, X-Ray line broadening from filed aluminium and wolfram, Acta Metall. 1 (1953) 22–31.
[48] M. Karolus, E. Łągiewka, Crystallite size and lattice strain in nanocrystalline Ni–Mo alloys studied by Rietveld refinement, J. Alloys Compd. 367 (2004) 235–238, https://doi.org/10.1016/j.jallcom.2003.08.044.
[49] S. Kumari, D.K. Singh, P.K. Giri, Strain anisotropy in freestanding germanium nanoparticles synthesized by ball milling, J. Nanosci. Nanotechnol. 9 (2009) 5231–5236, https://doi.org/10.1166/jnn.2009.1138.
[50] G.K. Williamson, R.E. Smallman III, Dislocation densities in some annealed and cold-worked metals from measurements on the X-ray debye-scherrer spectrum, Philos. Mag. 1 (1956) 34–46, https://doi.org/10.1080/14786435608238074.
[51] Y.H. Zhao, X.Z. Liao, Z. Jin, R.Z. Valiev, Y.T. Zhu, Microstructures and mechanical properties of ultrafine grained 7075 Al alloy processed by ECAP and their evolutions during annealing, Acta Mater. 52 (2004) 4589–4599, https://doi.org/10.1016/j.actamat.2004.06.017.
[52] R. Cunningham, S.P. Narra, C. Montgomery, J. Beuth, A.D. Rollett, Synchrotron-based X-ray microtomography characterization of the effect of processing variables on porosity formation in laser power-bed additive manufacturing of Ti-6Al-4V, JOM 69 (2017) 479–484, https://doi.org/10.1007/s11837-016-2234-1.
[53] A.M. Beese, B.E. Carroll, Review of mechanical properties of Ti-6Al-4V made by laser-based additive manufacturing using powder feedstock, JOM 68 (2016) 724–734, https://doi.org/10.1007/s11837-015-1759-z.